MEASUREMENT OF THE TEMPERATURE MARGIN IN HFDB02

G. Ambrosio, P. Bauer[1], E. Barzi, S. Feher, A. Godeke*, L. Imbasciati, J. Tompkins
Fermilab, Technical Division
*University of Wisconsin, Applied Superconductivity Center

In view of a future, post LHC hadron collider, Fermilab is developing high field accelerator magnets using Nb_3Sn superconductor. Two high field magnet designs have been developed and are currently in the prototyping stage. One of them, the one-layer, common coil dipole model, uses brittle Nb_3Sn superconductor in the react-and-wind approach. In view of the common coil magnet development a more general react-and-wind R&D program has been launched two years ago, aiming at a better understanding of the performance degradation of the brittle Nb_3Sn during the multiple technological steps from virgin strand to the magnet. The racetrack magnet program is part of the react-and-wind development program, whereby the performance degradation is measured in flat racetrack coils, assembled into a simple mechanical structure. The second racetrack magnet has been recently tested. The following note reports on temperature margin measurements performed on the second racetrack model. These measurements were obtained using a combination of a spot heater and a calibrated temperature sensor, fixed onto a turn of the magnet in close proximity to each other. The magnet was operated at a constant current below the short sample limit and the cable temperature was raised, sending a DC current through the spot heater, while measuring the temperature rise in the cable, until a quench occurred. The so found temperature margin can be related to the critical current in the particular spot where the spot heater and temperature sensor were located. Therefore the temperature margin measurement allows for an indirect measurement of the local performance limit of the magnet. The experimental results, as well as the critical surface implementations used to predict the temperature margin for a given strain state in the Nb_3Sn conductor are discussed in this note.

----

[1] e-mail: pbauer@fnal.gov

1) RACETRACK MODEL HFDB02

The racetrack magnet consists of two flat racetrack coils (Figure 1), wound using a pre-reacted Rutherford type cable made from Nb_3Sn superconductor strands and spliced internally with NbTi superconductor cables. The magnet was designed to achieve ~9 T, in order to study the behavior of coils fabricated with the react-and-wind technology by comparing the critical current degradation in the magnet with the degradation measured on wire and cable short samples. The magnet contains no iron because a simple mechanical structure was preferred to a larger and more complicated structure, which would allow iron in close proximity to the coils (iron outside the mechanical structure would have a very low efficiency). The coils have approximately 30 turns. The maximum field in the coil (9.02 T) is in the center (i.e. fifteenth turn) of the straight section (Figure 2).
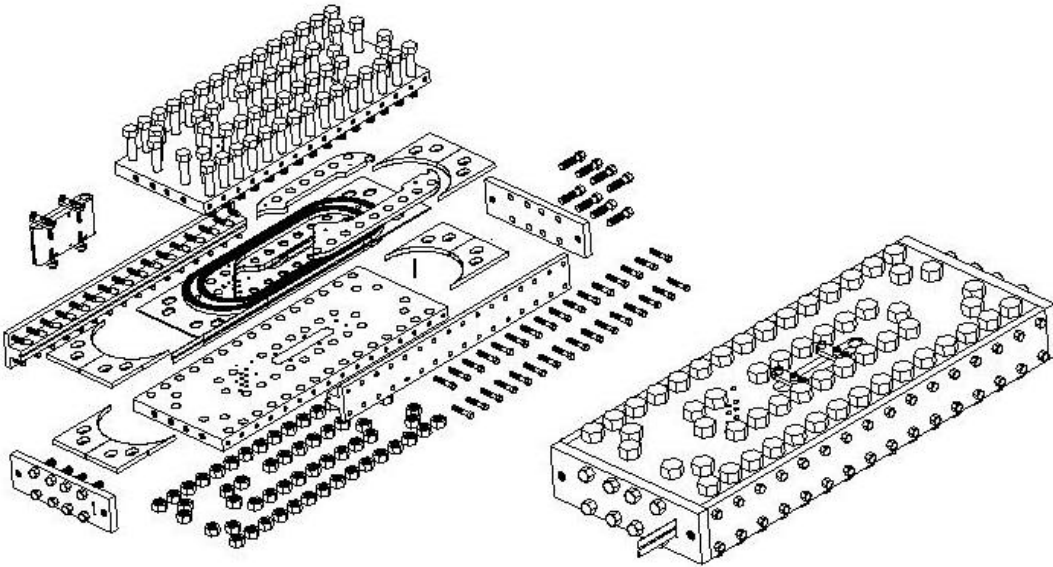

Figure 1: Racetrack, sketch of the mechanical structure.

The minimum inner bending diameter in the coil ends is 180 mm. The main components of the mechanical structure are two 40 mm thick stainless steel plates, which provide pre-stress and contain most of the magnetic forces. 57, 25 mm $\varnothing$, stainless steel bolts, pre-loaded to 3000 kg after magnet impregnation, should limit the coil separation to within 0.05 mm at maximum field. Side pushers provide vertical pre-stress and support by means of 32, 12 mm $\varnothing$ bolts. In the ends pre-stress and support is provided by 25 mm-thick, bolted end-plates. The plates, pushers and bolts are made of non-magnetic stainless steel. A 5 mm-thick G10 plate separates the coils. End parts are made of brass. All parts inside the coils, both in the ends and in the straight section, are made of G10. The NbTi cable connecting the coils is pre-shaped around a G10 rod and closed inside a G10 block. Pins are used to center the coil inserts and the inter-coil plate on the top of the main plate. After assembly, the magnet was vacuum impregnated with epoxy. After impregnation the external surface of the magnet was cleaned of epoxy, all bolts were extracted, cleaned, re-

inserted and pre-stress was applied. A more detailed description of the magnet design, the components and its assembly can be found in [1]. Figure 2 shows an instrumentation map of the HFDB02 model, indicating the position of the spot heaters, which were used in this study. The magnetic field at the location of the spot heaters can be read from the field map in *Figure 2*, which was computed for a magnet current of 17.58 kA. The field map shows that the spot heaters were not positioned in the peak field region (along the inner edge of the coil), but rather in a region of average field. The peak field and heater region load-lines are plotted in *Figure 14*).

Figure 2: Instrumentation map of racetrack HFDB02. The spot heaters are located at the upper right corner, inside edge of both coils, next to the temperature sensors (denoted as CX in the plot). A field map (calculated for 17.58 kA), including an indication of the heater location, is shown on the right.

2) MOTIVATION FOR THE TEMPERATURE MARGIN MEASUREMENTS

A quench history plot (Figure 3) reveals that the performance of the HFDB02 model was limited to ~12 kA, falling short of the expected short sample limit of ~16.5 kA (assuming a total of 20% degradation due to cabling and bending). The current understanding of the magnet performance gained from the analysis of voltage data, is that either a movement

3

in the lead end of the top coil or a localized cable damage is the cause of the performance limitation. The mechanical limitation could be related to a weak support of the lead end. Ramp-rate effects indicate a localized DC heating effect which could be explained by a severe damage of the cable in one or several spots. The quench voltage data indicate a massive quench affecting the entire outer 14 turns of the top coil, most likely originating in the lead end. With the performance limitation being of mechanical nature and/or localized, it is very likely that a higher performance limit, maybe even the short sample limit, could have been reached in the rest of the coil. The instrumentation of the HFDB02 model included 2 sets of spot heaters placed close to calibrated temperature sensors. This particular arrangement of heaters with adjacent temperature sensors made it possible to put the above statement to a test.
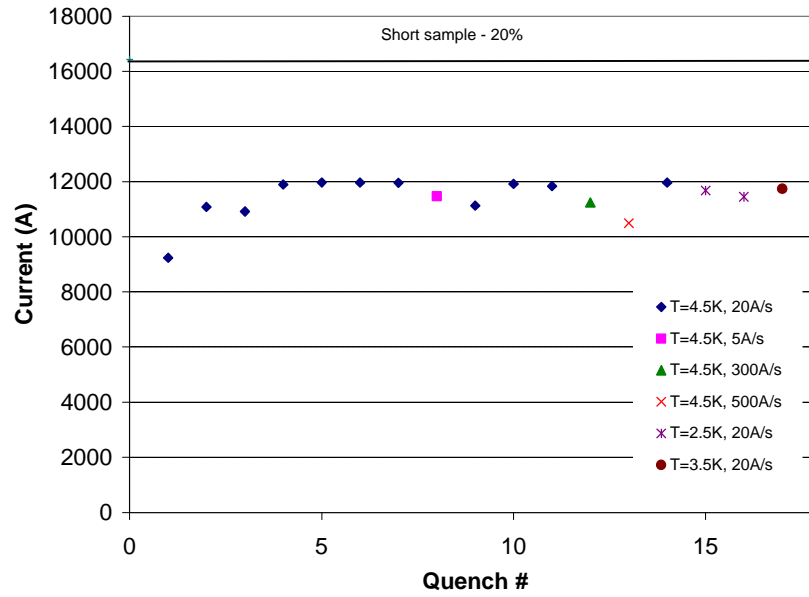

Figure 3: Quench history of HFDB02 during the first thermal cycle.

3) RESULTS OF THE TEMPERATURE MARGIN MEASUREMENTS

The indirect critical current measurement consisted in operating the coils at a constant current, below the limiting current of ~12 kA. Subsequently the cable temperature was raised, sending a DC current through the 2.5 cm long spot heater (covering the cable over its entire width), while measuring the temperature rise in the cable a few mm up-stream with a calibrated Cernox sensor, until a quench occurred (see sketch in Figure 4). The heater current was raised in small steps and the system was given time to establish equilibrium conditions after each step. The temperature at which a quench occurred in the cable, that is the critical temperature, can be, in conjunction with a critical surface parametrization, related to the potential critical current in the particular spots where the spot heaters and temperature sensors were located. The experimental results are shown in Figure 5. The procedure for the derivation of the potential critical current of HFDB02 from the temperature margin measurement is discussed in 5,6,7 and 8.
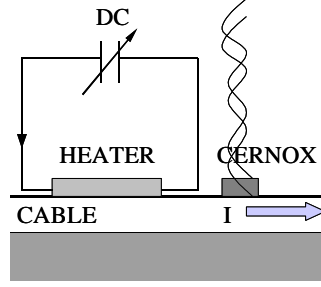
4

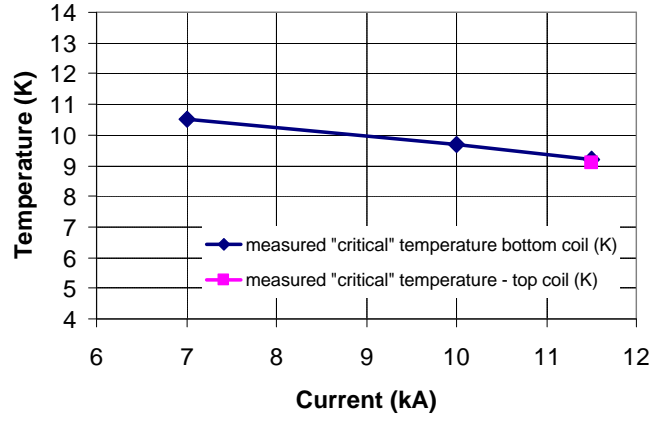Figure 4: Schematic of temperature margin measurement set-up.

Figure 5: Temperature margin measurement, quench temperature versus magnet current; bottom and top coil – raw data.

Due to the fact that the temperature margin measurement was conducted in a 4.5 K background, temperature gradients are expected to occur at the edges of the zone heated by the 2.5 cm long spot heater. The temperature sensor is placed ~1cm upstream from the heater, thus measuring a lower temperature than the peak cable temperature under the heater. The center to center distance between heater and temperature sensor is 16 mm. In addition, the temperature sensor is separated from the cable by a 0.254 mm thick layer of cable and ground insulation (consisting of 0.178 mm G10 and 0.076 mm Kapton). Therefore it was necessary to estimate the temperature difference between the cable hotspot and the temperature sensor, such as to relate a quench temperature to the Cernox data. A FE model, discussed in part 4, indicates a ~1.5 K temperature difference between cable hot spot and temperature sensor. Most of the temperature drop occurs along the cable, between the point facing the center of the spot heater and the point facing the center of the temperature sensor. The temperature drop through the layer of insulation separating the cable from the temperature sensor is comparatively small (~100 mK).

5

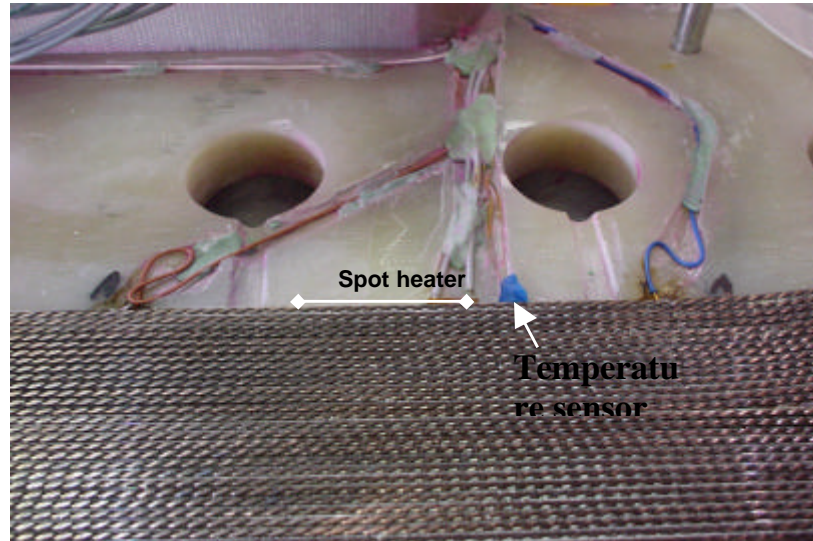## 4) FE MODEL OF THE TEMPERATURE MARGIN EXPERIMENT

Figure 6: Bottom coil in the spot heater region.

Figure 6 shows the section of the bottom coil with the spot heater. The edge-to-edge distance between the temperature sensor and the spot heater is 5 mm. The length of the sensor is about 3 mm, and the spot heater is 25 mm long. Using the finite element program ANSYS, the experiment was simulated with two complementary 2-D models. One model represents the region close to the spot heater from the same point of view as in Figure 6, that is the plane spanned by the x-axis along the cable and y-axis from cable to cable. The model is shown in Figure 7, together with the results of a simulation. Heat exchange with liquid helium at 4.5 K is implemented at the boundaries of the model. In reality, the heat exchange with helium occurs mainly through the stainless steel plates on top of the coils and the bolt-holes in the G10 island, which contain some helium. The main deficiency of this model, however, is related to the fact that the largest fraction of heat is exchanged into the direction perpendicular to the coils, through the main stainless steel plates and thus perpendicular to the plane of this model. To quantify the heat flux into the different directions a second 2-D model of the racetrack magnet (Figure 8) was built, which represents one quadrant of the cross section of the magnet. The x-axis runs along the width of the cable and the y-axis from cable to cable. The results of the second model show that the heat flux through the thick stainless steel plates represents ~80% of the total flux, the rest remaining within the coil plane. In fact, in the plane of the coils the heat is transported through the coils and G10 parts, which have a lower heat conductivity. During the experiment, the current in the spot heater was increased up to ~ 0.5-0.6 A, generating therefore (R_{heater}=2.3 Ω) a power of ~ 0.6-0.8 W. In this simulation, the heater current was set to 0.5 A. To calculate the temperature difference between the temperature sensor and the maximum temperature in the cable it is necessary to use model 1. To take into account the heat conducted away in the other directions model 1 was used, with a heater power which is only ~ 20 % of the actual, which corresponds to an input current ~ 40 % of the experimental heater current.
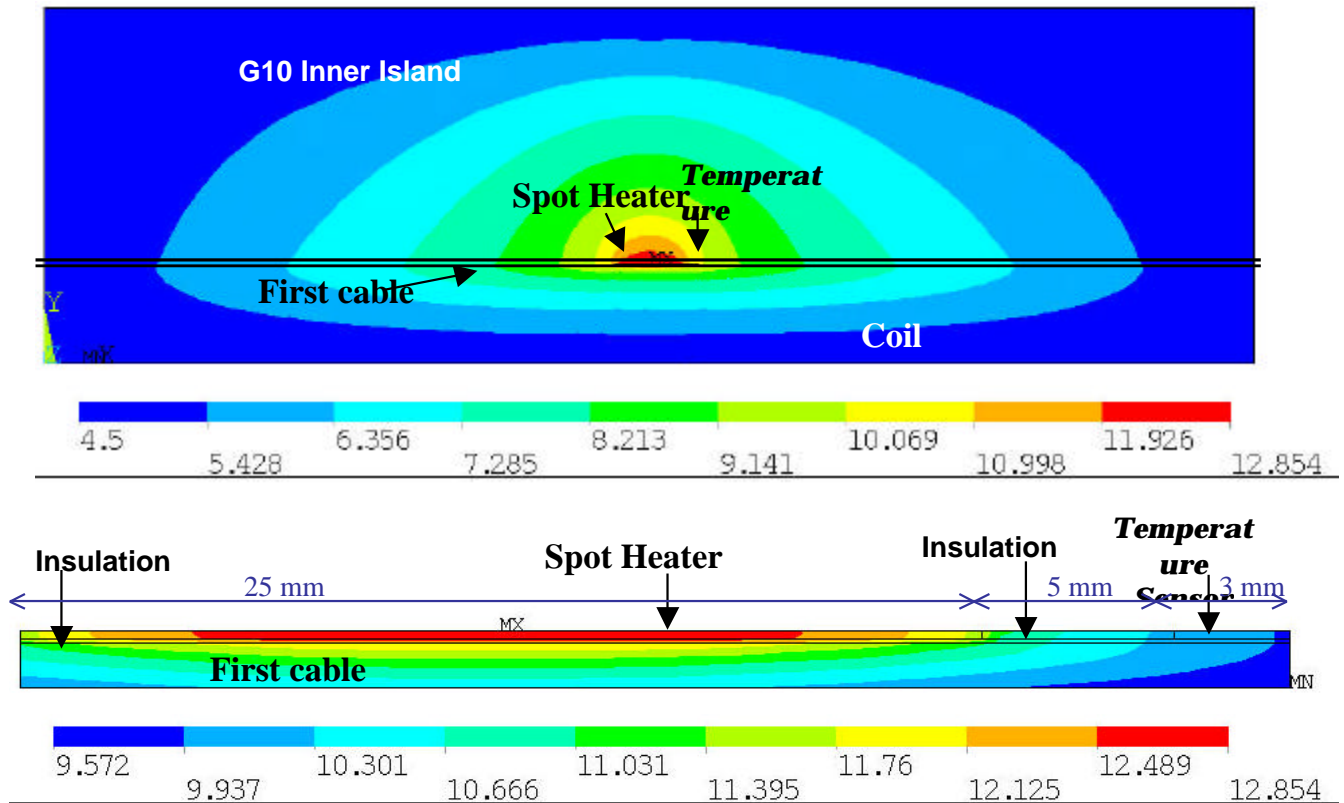
Figure 7: ANSYS model and temperature distribution (K), for 0.16 W heater power: complete model, top, and detail, bottom.
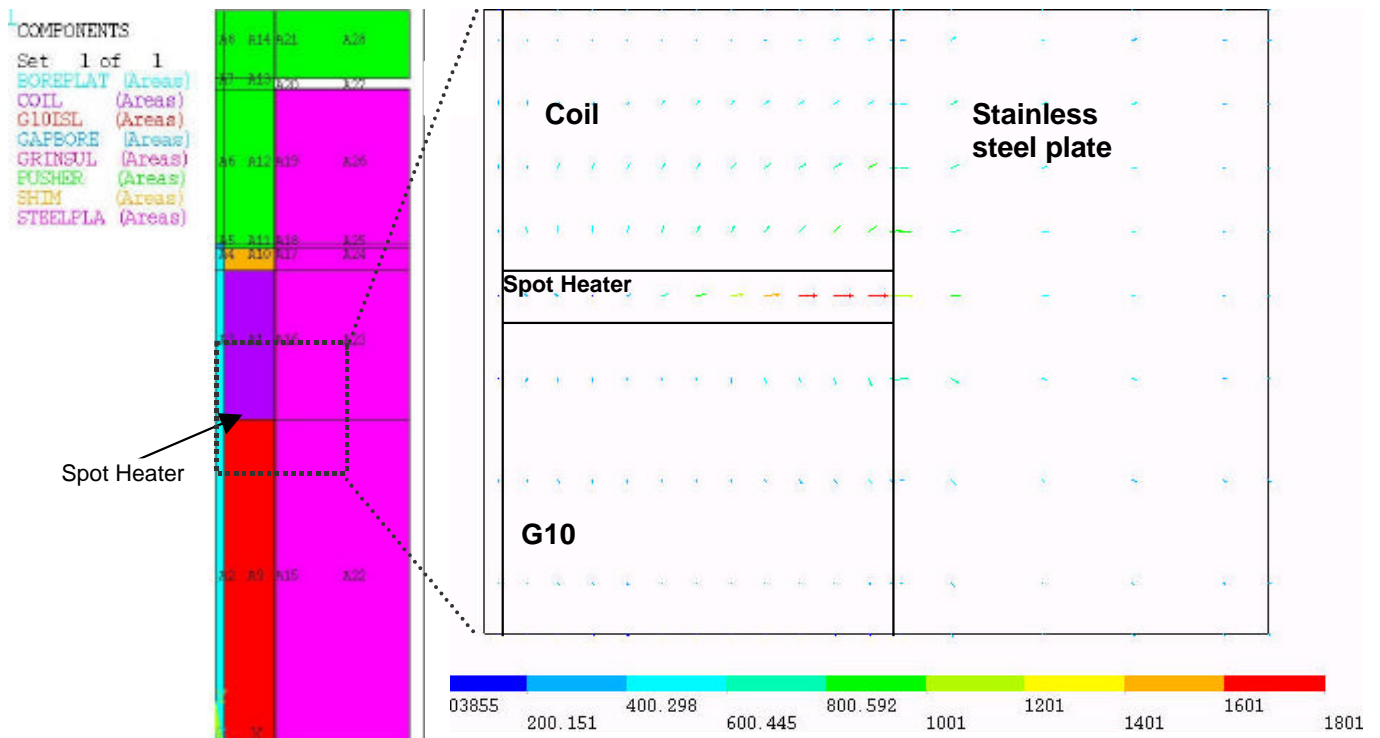

Figure 8: Second ANSYS model: complete model geometry, left. and the solution for a current of 0.5 A, showing the heat flux in the spot heater region, right.

Table 1: Summary of the simulations: input power, current and resulting temperatures.

ANSYS model results					
Spot heater model power (W)	0.11	0.13	0.16	0.18	0.21
Spot heater model current (A)	0.22	0.24	0.26	0.28	0.3
Sensor ave. temperature (K)	8.84	9.43	10.05	10.72	11.44
Cable max. temperature (K)	10.35	11.21	12.15	13.16	14.24
Temperature difference (K)	1.51	1.79	2.10	2.44	2.80

Table 1 lists the input power and current used in the model, together with the results of the calculation of the steady state temperature distribution. The simulations were performed at different heater powers.

Figure 9 shows a plot of the maximum temperature in the cable close to the spot heater as a function of the temperature in the temperature sensor (average temperature over the small area of model). A linear fit of this curve was then used to apply the correction to the measured values:

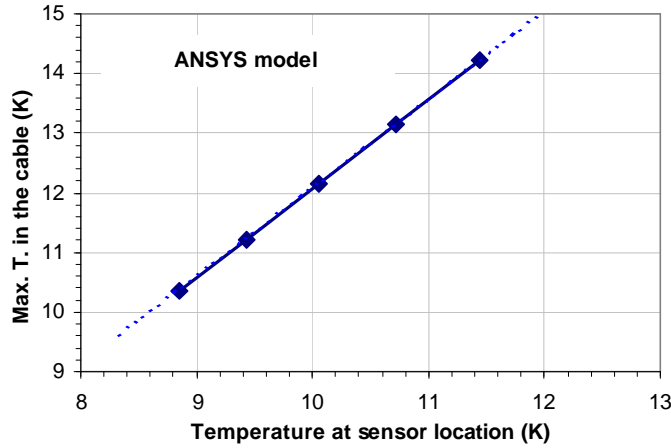$$T_{peak}^{cable} = 1.5 T_{sensor}(K) - 2.9\,K \tag{1}$$

Figure 9: ANSYS model results: maximum temperature in the cable as a function of the temperature in the sensor (average) temperature. Also shown is the linear fit, (1).

5) MODEL OF THE STRAIN EFFECT ON THE NB$_3$SN CRITICAL CURRENT

The following summarizes the critical surface implementations developed by Ekin/Summers, [2],[3], and some recent refinements presented by the Twente group, [4]. According to them the critical current density of Nb$_3$Sn as a function of magnetic field B, temperature T and strain ε is given with:

$$J_c(B,T,C_0,e) = \frac{C(C_0,e)b(T,e)^n}{BK(T,e)^g} S(e)^n f\left(\frac{B}{B_{c2}(T,e)}\right) \quad \left(\frac{A}{m^2}\right) \tag{2}$$

The strain dependence of the critical temperature T_c, critical field B_c and the current gauge constant C is usually written in terms of the strain function $S(e)$:

$$T_{c0}(e) = T_{c0m} S(e)^{\frac{1}{w}} \quad (K) \tag{3}$$

$$B_{c20}(e) = B_{c20m} S(e) \quad (T) \tag{4}$$

$$C(C_0, e) = C_0 S(e)^n \quad \left(\frac{AT}{m^2}\right) \tag{5}$$

where T_{c0m} and B_{c20m} are the critical temperature and field at zero strain. The critical current constants C_0 are defined differently in the Ekin/Summers and Twente models. They are related through:

$$C_0^{E/S} = \frac{C_0^T}{\sqrt{B_{c20m}}} \quad \left(\frac{AT^{1/2}}{m^2}\right) \tag{6}$$

Summer's refined temperature effect model is given with the K function:

$$K(T, e) = \left[1 - 0.31\left(\frac{T}{T_{c0}(e)}\right)^2 \left(1 - 1.77\ln\left(\frac{T}{T_{c0}(e)}\right)\right)\right], \tag{7}$$

such that the temperature dependence of the critical field can be written with b

$$b(T, e) = \left[1 - \left(\frac{T}{T_{c0}(e)}\right)^2\right] K(T, e), \tag{8}$$

as:

$$B_{c2}(T, e) = B_{c20}(e) b(T, e) \quad (T) \tag{9}$$

The Kramers pinning force factor is usually written in the following form:

$$f\left(\frac{B}{B_{c2}(T, e)}\right) = \left(\frac{B}{B_{c2}(T, e)}\right)^p \left[1 - \left(\frac{B}{B_{c2}(T, e)}\right)\right]^q \tag{10}$$

The material parameters used in (2)-(10) can be found in the following Table 2.
Different implementations of the strain function $S(e)$ have been proposed. First, Ekin, [2], proposed a strain function of the form (11), where a is a constant which he found to be

900 for compressive strain and 1200 for tensile strain and u is a material parameter (see Table 2).

$$S(\boldsymbol{e}) = \left[1 - a(|\boldsymbol{e}|)^u \right] \tag{11}$$

A recent, phenomenological model, the so-called deviatoric strain model, developed at Twente university, [4], describes the effect of strain on B_{c2}, T_{c0} and C with a strain function, that converges to the Ekin/Summers model in the limit of large strain.

$$S(\boldsymbol{e}) = \frac{1 - C_a \sqrt{(\boldsymbol{e})^2 + (\boldsymbol{e}_{0,a})^2}}{1 - C_a \boldsymbol{e}_{0,a}} \tag{12}$$

$\boldsymbol{e}$ is the equivalent, axial strain (including intrinsic and external strains), C_a the strain sensitivity, and $\boldsymbol{e}_{0,a}$ is the small strain (~0) at which the J_c/strain characteristic saturates. In the most general case the strain in the conductor is represented by a 3x3 matrix. The axial strain $\boldsymbol{e}$ in (12), however, can be derived from the 3D strain matrix using the deviatoric strain function defined in (13).

$$\boldsymbol{e}_{dev} = \frac{2}{3} \sqrt{(\boldsymbol{e}_x - \boldsymbol{e}_y)^2 + (\boldsymbol{e}_y - \boldsymbol{e}_z)^2 + (\boldsymbol{e}_z - \boldsymbol{e}_x)^2} \tag{13}$$

Table 2 gives a summary of the material and conductor parameters for state of the art wires. In some cases values measured on strands of the type used in the racetrack magnet (OST) are reported.

Table 2: Material and conductor parameters for the conductor used in HFDB02. In the cases in which two numbers are quoted, the first number refers to the Ekin/ Summers model, while the second number refers to the Twente model. Values measured on strands used for the racetrack magnet are indicated with an asterisk. The strain e is the axial, intrinsic strain only. Bending strain is not included. C_0, the main tuning parameter of the model was found via a fit of measured critical currents (Figure 11). The C_0 constant is in units of $AT^{0.5}/mm^2$ in the Summers model and AT/mm^2 in the Twente model. They are related with (6).

n	p	q	ν	γ	u	w
1	**0.5**	**2**	**2.5 / 2**	**2 / 1**	**1.7**	**3**
a	ε	C_a	$\varepsilon_{0,a}$	B_{c20m}	T_{c0m}	C_0
900	**-0.0029***	**39.12**	**0.0017**	**27.4**	**16.7**	**33500* / 185000***

Figure 10 shows a measurement of the critical current of an OST strand (of the type used in the racetrack magnet) as a function of axial strain. This measurement, performed at NIST, indicates that the filaments are at an intrinsic pre-compression of 0.29%. The intrinsic pre-compression of the filaments is the result of differential thermal contraction between filaments and matrix during cool-down from the reaction temperature to the operational temperature. With a choice of constants such as those stated in Table 2, the
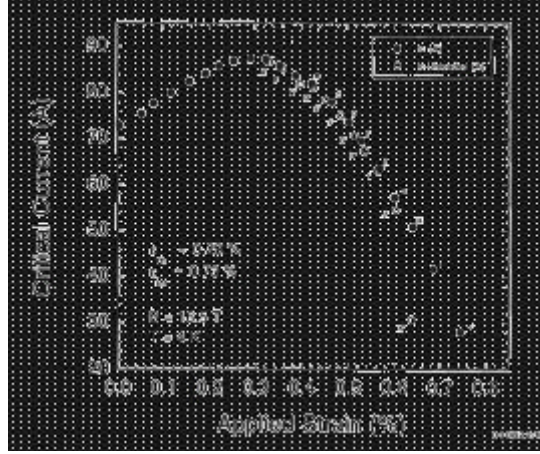
Figure 10: Critical current change as a function of longitudinal (tensile) strain. Measurement performed on billet OST/ORE/130 (thin barrier, 0.6 mm strand diameter). Note that the bending degradation measurements were performed on strands produced from a different billet, than the billet used in the fabrication of the racetrack conductor. The peak in this plot agrees with an intrinsic pre-compression of 0.29%. Measurements are courtesy of J. Ekin/NIST.

critical current density of an OST, MJR-process strand ($\varnothing$=0.7 mm, l=0.87), calculated with both models and compared to experimental data, is shown in Figure 11. It can be seen that the fit is satisfactory. The strain e used in the fit of the experimental critical current data takes into account differential thermal contraction of the titanium barrel with respect to the specimen as well as hoop-stress due to Lorentz-forces. The differential thermal contraction strain, e_{therm}, was estimated to be +0.1%. The hoop stress strain, e_{LF}, (which was neglected in the Twente model calculation) was calculated using the constant 0.005%/T/kA. It varies between +0.01% at 15 T to +0.03% at 9.5 T. This strain was added to the intrinsic pre-strain measured by Ekin, e_0 =0.29%.
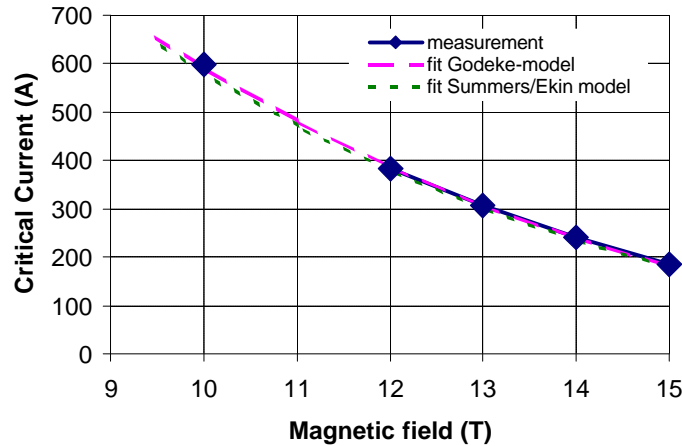

Figure 11: Fit of experimental critical current data (at 4.22K) measured on a strand sample for racetrack II (billet: OST/ORE-151). No self-field correction included.

11

6) CABLING AND BENDING DEGRADATION MEASUREMENTS ON STRANDS FOR RACETRACK II
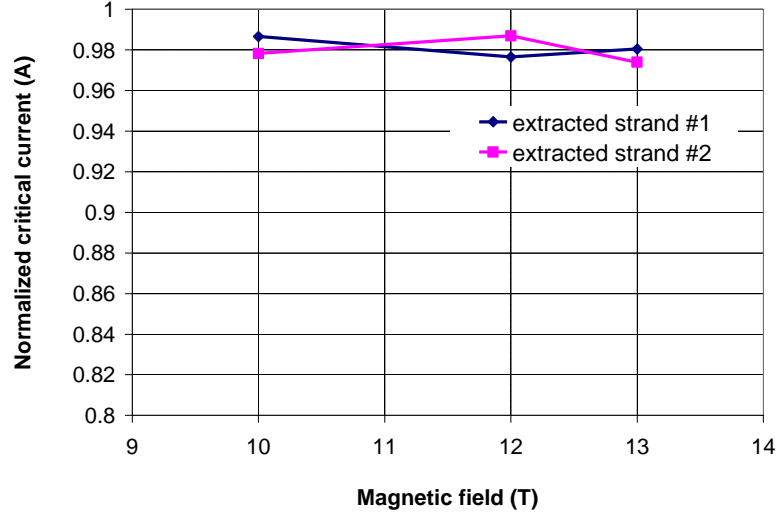

Figure 12: Degradation of the critical current due to cabling. Critical current of "extracted" samples normalized on the critical current of virgin samples. Cabling degradation measurement, billet OST/ORE 151.

A comparison of the critical current measured on a strand before ("virgin") and after cabling ("extracted" from a cable) allows to estimate the degradation of the critical current due to cabling. Such a measurement was performed on the conductor for HFDB02. The result, shown in Figure 12, indicates a very modest cabling degradation of the level of ~2%.

As part of the routine procedure in the racetrack preparation, bending strain effect measurements were performed on strands for the racetrack conductor. The measurement technique is discussed in detail in [5]. The measurements were performed for two different test-barrel diameters, producing a maximum bending strain of 0.245% and 0.48%. As was experimentally shown with ITER cables, [6], the critical current degradation due to bending of Rutherford type cables, is either determined by a single or double strand diameter. It is currently not possible to predict which case occurs in the magnet. That is the motivation for conducting bending strain effect measurements at two possible maximum bending strains. The two strains correspond approximately to the two possible maximum bending strains of the strand in a cable bent around the racetrack ends. The maximum bending strain, $\boldsymbol{e}_b$, occurs at the outermost layer of filaments and can be calculated with:

$$\boldsymbol{e}_b = \frac{\boldsymbol{f}}{2}\left(\frac{1 - R1/R2}{R1 - \boldsymbol{f}/2}\right) \tag{14}$$

from the distance of the outermost filament from the neutral fiber $\boldsymbol{f}/2$ and the bending radii before and after bending $R1$ and $R2$. The strain is compressive on the inside edge of
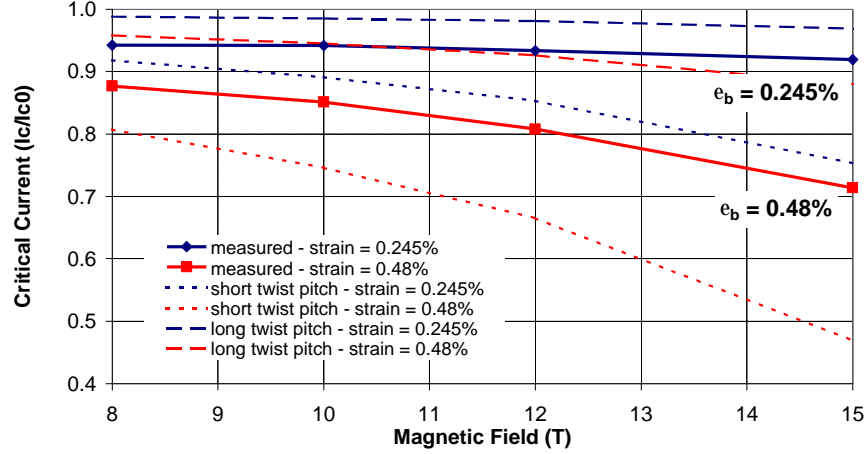
Figure 13: Measured, relative critical current degradation for two maximum bending strains on strands from the OST/ORE/139/B4 billet. Note that the bending degradation measurements were performed on strands produced from a different billet, than the racetrack conductor. The models leading to the calculation results are described in part 7).

the strand and tensile on the outside edge. The measurement results are shown in Figure 13. As can be seen in this plot the agreement between experimental data and two possible bending degradation models (the "short" and "long" twist pitch models) is not satisfactory. This issue will be discussed together with the bending degradation model in 7). Besides the maximum bending strain (as discussed next), the model calculations take into account axial strains, such as the differential thermal strain e_{therm} on the sample after cool-down on a Ti-barrel, the hoop strain on the conductor due to Lorentz-forces, e_{LF}, as well as e_0, the intrinsic strain.

7)   BENDING DEGRADATION MODEL

The dual nature of bending strain, tensile on one edge of the conductor and compressive on the other, together with the complicated geometry of a twisted, multifilament conductor, make the calculation of the critical current degradation in a strand due to bending difficult. Ekin, [2], presented a model to calculate the bending strain effect in two limiting cases, the short twist pitch, (17), and the long twist pitch limit, (18). In the long twist pitch limit, the current is shared from the strongly degraded filaments on the side of larger strain to the filaments with enhanced or less degraded critical current on the side of lower strain. Note that the intrinsic pre-strain is usually compressive, thus the region of lower degradation is at the outside of the bend, where the additional bending strain is tensile. The degradation is given by an average strain, which lies close to the intrinsic bending strain. In the short twist pitch limit such current sharing through the resistive matrix is not possible and the overall degradation of the critical current is given by an average strain, somewhere between the intrinsic strain and the sum of intrinsic strain and maximum bending strain.
As discussed before, the critical current reduction as a result of axial strain can easily be computed from (2), entering the intrinsic strain and other axial strain contributions (thermal, Lorentz-forces,..etc). The bending degradation, on the other hand, is factored

13

into the critical surface via a degradation factor *deg*. The degradation factor is obtained from the J_c function, (2), evaluated at strain e and normalized to its value at e=0. Ekin uses a simpler implementation of the critical surface, where $B_{c20}(T,e)\sim B_{c20}(e)$ and $K(T,e)$=1, to compute his degradation function, (15).

$$\deg(B,e) = \left(\frac{B_{c20}(e)}{B_{c20m}}\right)^{n-p} \left[\frac{1-\left(\frac{B}{B_{c20}(e)}\right)}{1-\left(\frac{B}{B_{c20m}}\right)}\right]^q \tag{15}$$

A short-coming of the simpler Ekin degradation function (15) is that it does not take into account the effect of strain on the critical temperature, T_c. A degradation factor calculated from the complete (Twente) J_c parametrization takes this effect into account, (16).

$$\deg(B,T,e) = \frac{J_c(B,T,C_0,e)}{J_c(B,T,C_0,0)} \tag{16}$$

The so-found degradation function, (15) or (16), is then integrated over the range of bending strains in the strand cross-section according to the two possible limiting cases mentioned above.

In the short twist pitch model the degradation factor *deg* is integrated between zero and the maximum bending strain e_b because, as a result of the pitch, every filament eventually crosses the region of stronger degradation between the neutral fiber and the compressed inside edge. To differentiate axial (e.g. intrinsic, thermal,..) from bending strain in the degradation formula the axial strain (which is the starting point of the integration) is denoted e_a.

$$\overline{\deg}(B,e_a,e_b)_{stp} = \frac{2}{e_b^2} \int_0^{|e_b|} y\,\deg(B,e_a - y)dy \tag{17}$$

In the long twist pitch model currents can share from the strongly degraded filaments to the less degraded filaments, such that the integration (or averaging) is performed over the complete maximum bending strain range $\pm\, e_b$ from the axial (i.e.) intrinsic strain e_a:

$$\overline{\deg}(B,e_a,e_b)_{ltp} = \frac{2}{pe_b^2} \int_{-|e_b|}^{|e_b|} \sqrt{e_b^2 - y^2}\, \deg(B,e_a + y)dy \tag{18}$$

Finally, to separate the bending strain effect from the effect of axial strains, the so found bending strain degradation is normalized on the degradation function $deg(B,T,e_a)$ as a result of axial strain only. This procedure is well suited, for example, for the particular

14

case of the simulation of strand bending on the critical current measurement barrel. The calculated bending degradation curves shown in Figure 13 were obtained from (19) in both the short and long twist pitch models (using Ekin's model (15) for the *deg* function).

$$\deg_{bend}(B,T,\boldsymbol{e}_a,\boldsymbol{e}_b) = \frac{\overline{\deg}(B,T,\boldsymbol{e}_a,\boldsymbol{e}_b)}{\deg(B,T,\boldsymbol{e}_a)} \qquad (19)$$

Taking into account (19), the critical current density degradation can be computed from (20), where the axial and bending strain contributions are factorized separately (note that the bending degradation depends on the axial strain as well as the bending strain).

$$J_c^{bend}(B,T,C_0,\boldsymbol{e}_a,\boldsymbol{e}_b) = J_c(B,T,C_0,\boldsymbol{e}_a) \times \deg_{bend}(B,T,\boldsymbol{e}_a,\boldsymbol{e}_b) \qquad \left(\frac{A}{m^2}\right) \qquad (20)$$

Figure 13 shows that in the particular case of the bending strain degradation measurements on the racetrack-II conductor, the model discussed here does not give a satisfactory result. This is unusual and demands a special investigation which could not be conducted in the frame of this study. The short twist pitch model data over-estimate the degradation, whereas the long twist pitch model underestimates it. The experimental results appear to be somewhere between the long and short twist-pitch cases. According to Ekin, [2], the characteristic length of current sharing is given by:

$$L = \sqrt{\frac{0.1}{n}}\sqrt{\frac{\boldsymbol{r}_m}{\boldsymbol{r}_c}}d \quad (m), \qquad (21)$$

where n is the I_c n-value (~30), $\boldsymbol{r}_c$ the "critical resistivity" (10^{-14} Ωm), $\boldsymbol{r}_m$ the transverse matrix resistivity and d the wire diameter (0.7 mm). The transverse matrix resistivity is difficult to estimate – according to [7] it can be anywhere between:

$$\boldsymbol{r}\frac{1-\boldsymbol{l}}{1+\boldsymbol{l}} < \boldsymbol{r}_m < \boldsymbol{r}\frac{1+\boldsymbol{l}}{1-\boldsymbol{l}} \quad (\Omega m) \qquad (22)$$

where $\boldsymbol{r}$ is the matrix resistivity. Assuming a low RRR (~10) copper matrix the current sharing length can be, depending on the transverse matrix resistivity, between 4 and 40 mm. The twist-pitch in the OST/ORE 151 billet, from which the racetrack II conductor was made, is ~10 mm. The OST/ORE 139 billet on which the bending degradation measurements shown in Figure 13 were performed, had the same pitch length. It is therefore possible that the conductor is in a "mixed" condition, between the long and short twist pitch limits of the Ekin model.
Other possible explanations have been recently brought forward. Among them the idea, that in (unprecedented) low copper content strands (such as those used for HFDB02), yielding of the copper matrix occurs during bending. During the yielding process the intrinsic strain state of the filaments in the matrix is altered. Assuming a smaller intrinsic

strain of the order of 0.1% would allow to reconcile the measurement results shown in Figure 13 with the short twist pitch model prediction.

Since there is currently no explanation for the apparent discrepancy between the intrinsic pre-compression found in the NIST experiments and the lower intrinsic strain consistent with the results of the bending strain experiments performed at FNAL (if the short twist pitch model is to be upheld), the following will present a separate discussion of two possible hypotheses. -1- a short twist pitch model with a 0.1% intrinsic compression and -2- a long twist pitch model with 0.29% intrinsic compression. Note that the strand bending degradation measurements shown in Figure 13 do not strictly agree with the long twist pitch model at $e_0=0.29\%$. As mentioned before, they appear to be in between the short and long twist pitch cases. Using the long twist pitch model in this context underestimates the degradation but is easier to implement than to define some "intermediate" model. Although, both the "simple" Ekin model, (15), and the complete ("complex") degradation function, (16), have been described here, only the "complex" implementation will be retained for the temperature margin simulations.

8) TEMPERATURE MARGIN MODEL

The temperature margin calculation proceeded via a graphical solution, as illustrated in Figure 14. The calculated temperature margin is the temperature at which the calculated critical current becomes equal to the measurement current in the temperature margin measurements (7, 10 and 11.5 kA) at the magnetic field in the "hot spot". The measurement currents are plotted along the "hot spot" load-line (see Figure 14) and the critical current curve is brought to intersection with the load-line, therefore taking into account the change of magnetic field at the spot heater location with the critical current in the conductor. The critical current is calculated with the J_c model, (2), discussed in 5). The Twente implementation has been chosen since it was verified on state of the art conductors. The bending degradation effect is calculated according to the recipe given in chapter 7). The cabling degradation discussed in 6) is included as well. A graphical solution for the expected temperature margin was sought for a variety of different models: the short twist pitch model (at 0.1% intrinsic strain, as discussed in 7)) and long twist pitch model (at 0.29% intrinsic strain, as discussed in 7)), with single-strand and double-strand maximum bending strain e_b. These issues were discussed in greater detail in 6 and 7. Finally, the two variations of the bending degradation model, (15) and (16), affect the outcome of the calculations as well. The simpler model, as proposed by Ekin, [2], calculates the degradation, assuming that the strain affects only B_{c2}, whereas the complete model, (16), takes into account as well the strain effect on T_c. Only the data calculated with the complete model are shown. Table 3 lists all cases that were analyzed. The calculated temperature margins are shown in Figure 15.
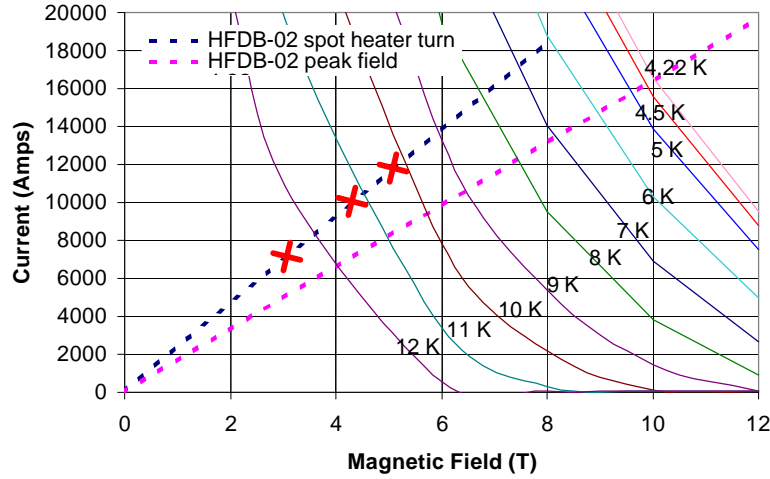
Figure 14: Example of graphical temperature margin calculation. Shown are the three measurement currents, the hot spot load line and the critical currents (calculated with (2) in the Twente implementation) at different temperatures between 4.22 K and 12 K. The critical current calculation includes a 3% cabling degradation. Since this plot was produced only for explanatory purposes, the bending degradation effect was calculated using a simplified model, assuming an "equivalent" bending strain of 0.48/2% inserted directly into (2) instead of using the procedures presented in chapter (7).

Table 3: Different cases that were modeled. The results are shown in Figure 15.

Case	Max bend strain ε_b	Model - pitch	Model	Intrinsic strain ε_0
1	0.245%	short	complex	0.1%
2	0.48%	short	complex	0.1%
3	0.245%	long	complex	0.29%
4	0.48%	long	complex	0.29%

Figure 15 shows a summary of the predicted temperature margins. First, it can be seen that the short twist pitch model, with the 0.1% intrinsic strain, is more sensitive to the bending strain. It yields the largest margin for the smaller bending strain (0.245%) and the smallest margin for the larger bending strain (0.48%). The long twist pitch model temperature margin prediction is relatively insensitive to the bending strain. The predictions based on the "simple" model produce larger margins. These results are not shown here for reasons discussed above. Although the underlying critical current variations can be large, all predicted temperature margin data fall into a relatively narrow band of ~0.5 K width. This is explained by the load line effect. The penalties for reduced critical currents are much smaller along the load line, than in a fixed back-ground field, since the field in the magnet drops as the critical current in the conductor is reduced, which in turn raises the critical current.
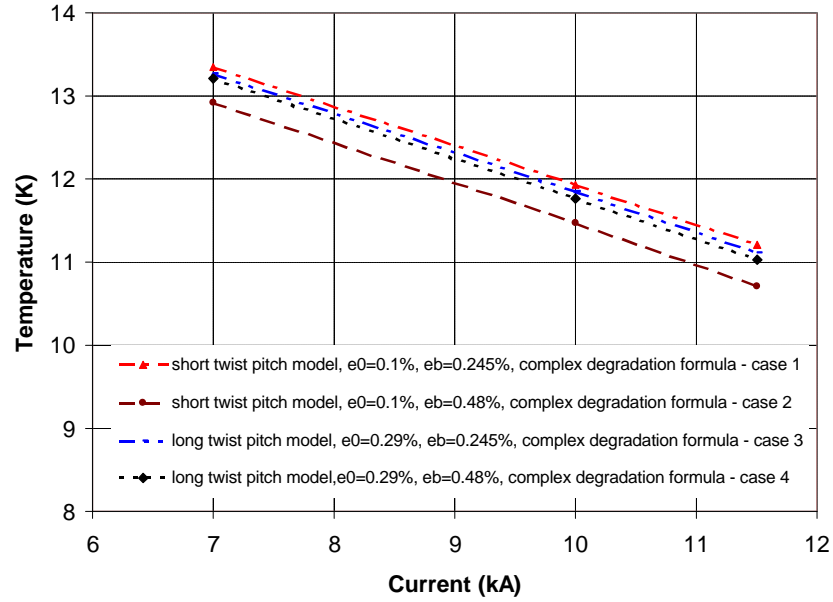
Figure 15: Temperature margin calculated with different models (see Table 3).

9) COMPARISON OF MODEL AND MEASUREMENTS

Figure 16 shows that all degradation models agree well with the ("corrected", see chapter 4) temperature margin measurements. The measurements coincide with the lower edge of
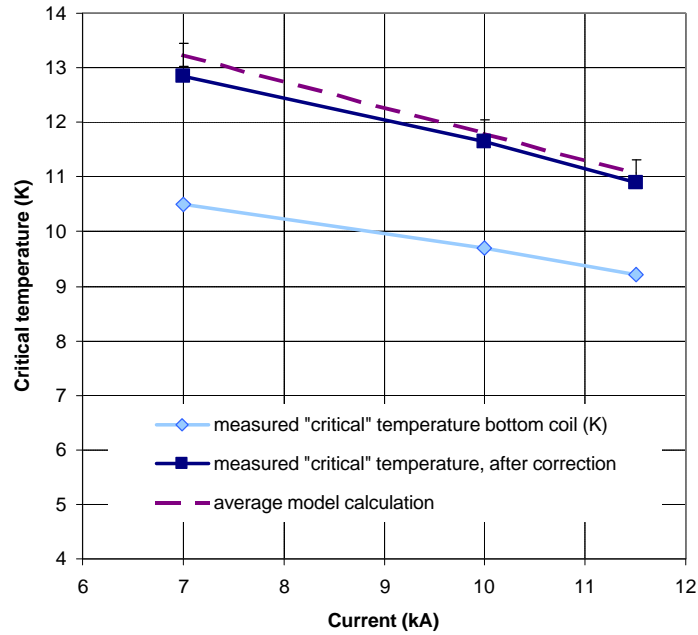

Figure 16: Comparison of temperature margin measurements and model predictions. The model predictions are represented by an "average" and "error" bars to show the variation. The model data are shown explicitly in Figure 15.

the band of model predictions. This implies that the result of the temperature margin measurement is consistent with the expected degradation in the cables due to cabling and bending. It also implies that, due to the "load-line compression", the temperature margin measurement cannot discriminate between the one- or two-diameter maximum bending strain degradation. The simple/complex degradation models yield significantly different results (the results from the "simple" model are not shown, but are generally giving larger temperature margins). The temperature margin measurement results appear to be more consistent with the predictions obtained on the basis of the complex model.

10) PREDICTION OF THE SHORT SAMPLE LIMIT OF HFDB02

Different critical surface models including the effect of bending strain on the critical current were used to predict the local short sample limit of HFDB02. The models were thus "calibrated" in a comparison with the experimental temperature margin data (see chapter 9). Taking into account the peak field load-line in HFDB02 (see Figure 14), the short sample limit could be predicted, once confidence had been gained in the critical surface models. Such short sample limit predictions are shown in Figure 17 for the different models. The models are discussed in detail in chapter 9. The estimated short sample limits are between 17100 A and 18100 A. This corresponds to a maximum critical current degradation in the conductor of ~10%. The highest current achieved in HFDB02 is indicated as well in the plot.
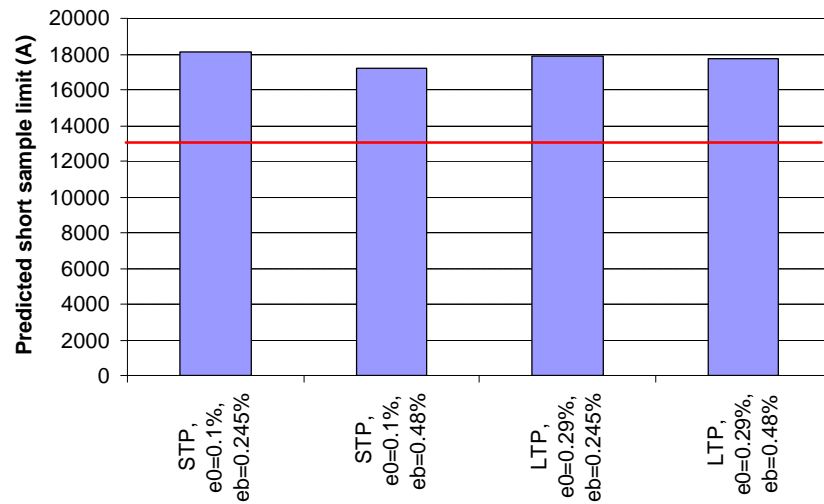

Figure 17: Short sample limits of HFDB02, derived from the temperature margin calculation using different possible models: The short twist pitch model (for both possible maximum bending strains) is based on 0.1% intrinsic strain. The long twist pitch model (for both possible maximum bending strains) is based on 0.29% intrinsic strain. All calculations were performed using the "complex" model. The best performance of HFDB02 is indicated by a line (12.7 kA in the second thermal cycle).

References:

19

[1]   G. Ambrosio et al., "*Development of a Nb3Sn Racetrack Magnet using the React and Wind Technology*", Proceedings of the ICEC 2001, Madison, WI, U.S.A.;

[2]   J. W. Ekin, "*Strain Scaling Law and the Prediction of Uniaxial and Bending Strain Effects in Multifilamentary Superconductors*", Proceedings of the Special Topic ICMC on Filamentary A15 Superconductors, M. Suenaga, A.F. Clark, editors, Plenum Press NY 1980, p. 187

[3]   L.T. Summers, M.W. Guinan, J.R. Miller, P.A. Hahn, "*A Model for the Prediction of Nb3Sn Critical Current as a Function of Field, Temperature, Strain and Radiation Damage*", Proceedings of the 1990 Applied Superconductivity Conference, Snowmass, Co, 1990;

[4]   A. Godeke, H.J.G. Krooshoop, H.G. Knoopers, B. ten Haken, H.H.J. ten Kate, "*Experimental Verification of the Temperature and Strain Dependence of the Critical Properties in Nb3Sn Wires*", IEEE Transactions on Applied Superconductivity, Vol. 11, No. 1, pp. 1526-1529, March 2001;

[5]   G. Ambrosio et al., "*Study of the React and Wind Technique for a Nb3Sn Common Coil Dipole*", Proceedings of the 16th Magnet Technology Conference, Florida, Sept. 1999;

[6]   P. Bauer et al., "*Fabrication and Testing of Rutherford-Type Cables for React and Wind Accelerator Magnets*", Proceedings of the 2000 Applied Superconductivity Conference, Virginia Beach, VA, Sept. 2000;

[7]   W.J. Carr, "*AC-loss and Macroscopic Theory of Superconductors*", Gordon&Breach, 1983;